



**CHALMERS**  
UNIVERSITY OF TECHNOLOGY

## **Discrete-Ordinates Modelling of the Radiative Heat Transfer in a Pilot-Scale Rotary Kiln**

Downloaded from: <https://research.chalmers.se>, 2024-04-24 10:21 UTC

Citation for the original published paper (version of record):

Gunnarsson, A., Andersson, K., Adams, B. et al (2020). Discrete-Ordinates Modelling of the Radiative Heat Transfer in a Pilot-Scale Rotary Kiln. *Energies*, 13(9).  
<http://dx.doi.org/10.3390/en13092192>

N.B. When citing this work, cite the original published paper.

## Article

# Discrete-Ordinates Modelling of the Radiative Heat Transfer in a Pilot-Scale Rotary Kiln

Adrian Gunnarsson <sup>1,\*</sup>, Klas Andersson <sup>1</sup>, Bradley R. Adams <sup>2</sup> and Christian Fredriksson <sup>3</sup>

<sup>1</sup> Division of Energy Technology, Department of Space Earth and Environment, Chalmers University of Technology, 41296 Gothenburg, Sweden; klon@chalmers.se

<sup>2</sup> Mechanical Engineering Department, Brigham Young University, Provo, UT 84602, USA; brad.adams@byu.edu

<sup>3</sup> LKAB, Box 952, SE-971 27 Luleå, Sweden; christian.fredriksson@lkab.com

\* Correspondence: adriang@chalmers.se

Received: 24 March 2020; Accepted: 28 April 2020; Published: 1 May 2020



**Abstract:** This paper presents work focused on the development, evaluation and use of a 3D model for investigation of the radiative heat transfer in rotary kilns. The model applies a discrete-ordinates method to solve the radiative transfer equation considering emission, absorption and scattering of radiation by gas species and particles for cylindrical and semi-cylindrical enclosures. Modelling input data on temperature, particle distribution and gas composition in the radial, axial and angular directions are experimentally gathered in a down-scaled version of a rotary kiln. The model is tested in its capability to predict the radiative intensity and heat flux to the inner wall of the furnace and good agreement was found when compared to measurements. Including the conductive heat transfer through the furnace wall, the model also satisfactorily predicts the intermediate wall temperature. The work also includes a first study on the effect of the incident radiative heat flux to the different surfaces while adding a cold bed material. With further development of the model, it can be used to study the heat transfer in full-scale rotary kilns.

**Keywords:** radiative heat transfer; rotary kiln; discrete-ordinates method; experiments and modelling

## 1. Introduction

Rotary kilns are cylindrical, tilting and slowly rotating furnaces, and the first patented invention resembling a rotary kiln was created in 1885 by Frederick Ransome, which was introduced to the cement industry [1]. Since then, the rotary kilns have been developed and are still used for cement production and several different other industries, such as pulp and paper and for iron ore pelletizing. The unit operation of a rotary kiln is mainly heat treatment of a solid bed material passing from the higher to the lower end of the kiln as the kiln is rotating with a luminous flame along the kiln axis. The heat transfer within the kiln is complex, since it not only includes convective, conductive and radiative heat transfer, but heat is also transferred in the angular and axial directions as the wall rotates and the bed mixes. Additionally, the bed material may be reactive and heat addition or loss from reactions should then be considered.

Several researchers have examined the heat transfer mechanisms within the kiln freeboard, bed material and walls. Experimental data from full-scale rotary kilns are, however, difficult to sample—mainly due to the large dimensions and the rotation of the kilns. Many studies have therefore focused on the development of different models, while others have conducted experiments in smaller furnaces. Cross and Young [2] examined flame characteristics and pellet throughput in a rotary kiln for oil and gaseous flames employing a one-dimensional flame model assuming grey radiative properties. Gorog et al. studied the radiative heat transfer in rotary kilns, with and without luminous flames,

as well as the regenerative heat transfer from the kiln wall while varying parameters such as the fuel type or temperature and oxygen enrichment of the secondary air [3–5]. Their work showed the computational errors associated with assuming grey properties by comparing results with calculations using a non-grey equimolar  $\text{CO}_2/\text{H}_2\text{O}$  mixture for the freeboard gas. Thornton and Batterham [6] developed a one-dimensional dynamic model of the radiative heat transfer and bed mixing in a rotary kiln. Barr et al. [7,8] studied a pilot-scale rotary kiln and the heat treatment of different solid materials. They developed a cross-section model of the radiative heat transfer in the rotary kiln for a natural gas flame with a reacting bed material using secondary air at ambient temperature. Boateng and Barr [9] developed a quasi-3D model of the thermal transport in a rotary kiln by comprising a 1D axial model together with a 2D model of the rotary kiln cross-section for the bed material. Several researchers have also studied the conductive heat transfer between the wall and bed material [10–13] as well as the convective heat transfer between the freeboard and the wall and bed materials [14]. The movement of the bed material, the different modes of heat transfer as well as the impact from different parameters on heat transfer in a rotary kiln, such as the temperature dependent radiative emissivity of different materials, has been summarized by Specht [15]. Several researchers have also developed different computational fluid dynamics (CFDs)-based models in order to model full-scale rotary kilns [16–19]. While such models can be used to provide valuable information of various processes, they rely on predictions of gas and surface temperatures, which can increase their uncertainty relative to measured properties.

This work focuses on rotary kilns used by the Swedish mining company Luossavaara-Kiirunavaara Aktiebolag (LKAB) for iron ore pelletizing, in which preheated iron ore pellets are further heated, oxidized and sintered as they move through the kiln, which has a total length of approximately 34 m and an inner diameter of 5.5 m. The bed of iron ore pellets constitutes approximately 10% of the kiln volume and the heat required by the process is mainly supplied from the suspension-fired combustion of fossil coal at a range of 35–40  $\text{MW}_{\text{th}}$ , with the burner positioned at the lower end of the kiln. The heat is mainly transferred to the pellet bed and kiln walls from the long jet flame due to radiation. High oxygen concentrations and gas temperatures of the freeboard gas are desired to promote oxidation of magnetite to hematite, achieved by preheating large volume flows of secondary air. The gas stream leaving the rotary kiln holds a temperature within the range of 1150–1250 °C and an oxygen concentration of approximately 16% [20]. The heated pellets enter the rotary kiln at temperatures slightly lower than the outgoing gas temperature and leave the rotary kiln at approximately 1270 °C [20], depending on the fuel used. The hot bed of pellets falls down to a cooler and is cooled with air passing through the bed. The air leaving the cooler is introduced as secondary air to the rotary kiln at a temperature of approximately 1050 °C. A more detailed description of LKAB's process can be found in the work by Jonsson et al. [21].

The use of coal as fuel results in large emissions of carbon dioxide and, due to the concerns of an increased global greenhouse effect, there is an urgent interest to switch to less carbon-intensive fuels. However, since the control of the kiln and the flame conditions are critical to achieve a high-quality product, it is necessary to consider how a change in fuel may affect the heat transfer within the rotary kiln, or rather, how to minimize eventual effects on the product. The aim of this work is to improve the understanding of the heat transfer process in rotary kilns using solid fuels, since quantitative knowledge on this is rather limited today. Here, the radiative heat transfer is examined for a stationary kiln, and modelling results are compared to measurement data gathered from a 580  $\text{kW}_{\text{th}}$  pilot-scale furnace in order to validate the model. The modelled and measured incident radiative heat fluxes to the inner wall of the furnace are of main interest, since they correspond to the heat transferred to the bed of iron ore pellets. Calculated radiative intensities and wall temperatures are also of interest in order to perform a first validation of the model.

## 2. Methodology

In the rotary kiln, heat is transferred to the iron ore pellet bed due to thermal radiation, convection and conduction within the bed and from the wall. With a long and luminous flame, the total heat transfer within the kiln is, however, considered to be dominated by radiation [1]. The need for an accurate and detailed model of the radiative heat transfer within the kiln to achieve a better understanding of the process and the total heat transfer is therefore obvious.

In this work, the radiative heat transfer is modelled and studied in three dimensions using a discrete-ordinates method (DOM) solving the radiative transfer equation (RTE) for cylindrical and semi-cylindrical enclosures. Originally, the DOM gained interest in the work of Carlson and Lathrop [22], solving neutron transport problems in different geometries. Since then, the DOM has been applied to and optimized for different radiative heat transfer problems; see, e.g., the review paper of Coelho [23]. Applying a DOM, the examined enclosure is divided into a number of three-dimensional cells and the RTE is solved for a set of weighted discrete directions for each cell. The DOM has been successfully used in previous studies of different cylindrical enclosures [24–26] as well as more complex geometries [27–31].

The authors have previously published a paper on the heat transfer modelling within a full-scale rotary kiln for iron ore pelletizing using a DOM [32], and the aim of this work is to describe the detailed radiative heat transfer model used, for a pilot-scale rotary kiln, and validate it by comparing it with measurement data. The developed model and treatment of the radiative heat transfer, in three dimensions, including emitting gases and fuel particles, were previously presented by the authors at the 6th International Conference on Computational Thermal Radiation in Participating Media [33] and have been further developed in this work to include the heat transfer through the furnace wall and an iterative solution of the inner wall temperature and the incident radiative heat flux. The authors have also applied a discrete transfer model (DTM) to study the radiative heat transfer in earlier studies for different cylindrical furnaces with satisfactory results while assuming axisymmetric flames [34,35]. The DOM has, however, been shown to be more economical and studies of non-axisymmetric systems of a whole furnace (in 3D) are more easily implemented in comparison to the DTM [36]. The modelling approach is described in more detail below.

The model in itself is not predictive of the combustion conditions within the pilot-scale furnace but can be used with advantage to study the radiative heat transfer properties in an industrial-scale rotary kiln in detail. Given an input data set of temperature, gas and particle concentrations, as well as surface properties, sensitivity analysis of certain parameters can be conducted to gain additional insight into the heat transfer process. The model can be used in future work as a submodel in a more comprehensive model, coupling the radiative heat transfer with gas, particle, and energy transport as well as combustion reactions in order to provide a more comprehensive predictive tool.

Input data for the model were gathered from experiments comprising temperature, gas composition and particle concentration in a rotary kiln pilot-scale furnace with a thermal input of 580 kW<sub>th</sub> and using a carbon-rich coal as fuel.

### 2.1. Modelling

The radiative transfer equation (RTE) describes how the radiative intensity,  $I$ , changes along a direction  $\hat{s}$ , while it accounts for the contributions from emission, absorption, and scattering into and away from the said direction. The RTE may be expressed for a given wavenumber,  $\nu$ , as:

$$\frac{dI_\nu}{ds} = \kappa_\nu I_{b\nu} - (\kappa_\nu + \sigma_{s\nu}) I_\nu + \frac{\sigma_{s\nu}}{4\pi} \int_0^{4\pi} I_\nu(\hat{s}_m) \Phi_\nu(\hat{s}_m, \hat{s}) d\Omega_m \quad (1)$$

where  $\kappa_\nu$  and  $\sigma_{s\nu}$  are the absorption and scattering coefficients for the present medium, respectively, and  $I_\nu(\hat{s}_m)$  is the spectral intensity scattered into direction  $\hat{s}$  from a small ray originating from direction  $\hat{s}_m$  depending on the scattering phase function,  $\Phi_\nu$ , over the solid angle  $d\Omega_m$ .

Considering a rotary kiln, the modelled enclosure will be defined by the cylindrical wall and the present bed material, i.e., a semi-cylindrical enclosure. To simplify the geometry of the enclosure, the bed material is assumed to be evenly distributed along the furnace axis and may then be approximated as a plane, as previously done by Thornton and Batterham [6]. While discretizing the enclosure into cells, the radial angle between two cells ( $\Delta\omega$ ) was kept constant and due to the geometry of the enclosure, two different cell types will be present in the DOM, here referred to as type I and II, as is shown in Figure 1. The total number of cells used in the DOM is given by:  $n_{tot} = n_r \cdot n_\psi \cdot n_z$ , where  $n$  represents the number of cells in the radial ( $r$ ), angular ( $\psi$ ), and axial ( $z$ ) directions.

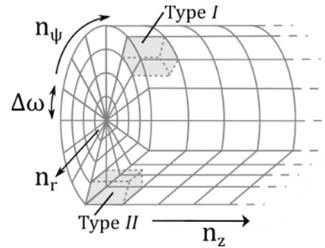


**Figure 1.** Schematic example of the cell discretization for a semi-cylindrical enclosure resembling a rotary kiln with a bed material approximated as a plane.

The radiative intensity to each cell node is calculated for a set number of directions, derived according to an  $S_N$  approximation, where  $N$  denotes the number of different direction cosines used for each principal direction,  $m$ , such that the total number of directions is given by:  $N \cdot (N + 2)$ . For the cylindrical and semi-cylindrical enclosures of a rotary kiln, the RTE may be expressed in terms of angular coordinates [25], according to:

$$\begin{aligned} \frac{\mu_m}{r} \frac{\delta(rI_m)}{\delta r} + \frac{\eta_m}{r} \frac{\delta I_m}{\delta \psi} + \xi_m \frac{\delta I_m}{\delta z} - \frac{1}{r} \frac{\delta(\eta_m I_m)}{\delta \phi} \\ = -(\kappa + \sigma_s)I_m + \kappa I_b + \frac{\sigma_s}{4\pi} \int_{4\pi} P(\Omega, \Omega') I_{m'} d\Omega' \end{aligned} \quad (2)$$

where  $\xi_m$ ,  $\eta_m$  and  $\mu_m$  are direction cosines for a ray travelling along the discrete direction  $\hat{s}_m$ , according to Figure 2.

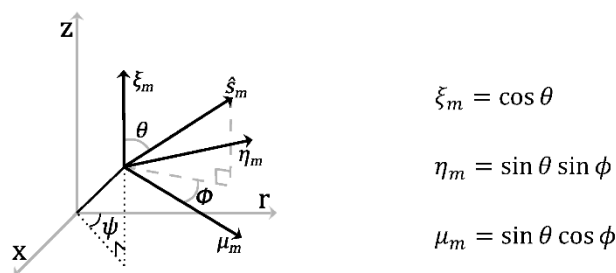


**Figure 2.** The direction cosines ( $\xi_m$ ,  $\eta_m$  and  $u_m$ ) for the discrete direction  $\hat{s}_m$ , where  $\theta$  and  $\Phi$  are the polar and azimuthal angles, respectively, and  $\psi$  is a space variable in the azimuthal direction.

The ordinates may be positive or negative with respect to the spatial coordinate system and a weight,  $w_m$ , is related to each quadrature set of ordinates to cover the whole sphere of  $4\pi$  sr from a point according to Equation (3). The quadrature sets are further constructed in a way to be invariant if rotated  $90^\circ$  and are described more thoroughly by Fiveland [37].

$$\begin{aligned}
 \xi_m \hat{i} + \eta_m \hat{j} + \mu_m \hat{k} &= \hat{s}_m \\
 \xi_m^2 + \eta_m^2 + \mu_m^2 &= 1 \\
 \sum_{m=1}^N (\xi_m^2 + \eta_m^2 + \mu_m^2) w_m &= 4\pi sr
 \end{aligned} \tag{3}$$

With an increasing  $N$  value, the number of rays increases along with the computational power required to solve the RTE. According to Fiveland [37], the angular discretization with the  $S_4$  approximation may yield reasonable enough solutions for some systems, while higher values require considerably more numerical effort. It should be noted, however, that the DOM may suffer from ray effects, which can be reduced by an increased number of discrete directions [23]. For this reason, the  $S_8$  approximation is used in this work. Table 1 lists numerical values of the discrete cosines and weights used, collected from the work of Modest [36].

**Table 1.** Discrete cosines and weights used for the  $S_8$  approximations [36].

$\xi_m$	$\eta_m$	$\mu_m$	$w_m$
0.1422555	0.1422555	0.9795543	0.1712359
0.1422555	0.5773503	0.8040087	0.0992284
0.1422555	0.8040087	0.5773503	0.0992284
0.1422555	0.9795543	0.1422555	0.1712359
0.5773503	0.1422555	0.8040087	0.0992284
0.5773503	0.5773503	0.5773503	0.4617179
0.5773503	0.8040087	0.1422555	0.0992284
0.8040087	0.1422555	0.5773503	0.0992284
0.8040087	0.5773503	0.1422555	0.0992284
0.9795543	0.1422555	0.1422555	0.1712359

By employing the angle between two cells in the angular direction,  $\Delta\omega$ , Equation (2) is solved by multiplying cell types *I* and *II*, respectively, with the expressions given by Equation (4):

$$\begin{aligned}
 \text{Type I} & \quad 2\pi r \, dr \, dz \, d\psi \\
 \text{Type II} & \quad r \frac{1}{\cos^2(\Delta\omega)} \, dr \, d\psi \, dz
 \end{aligned} \tag{4}$$

and integrating over the volume elements for each cell type. For both cell types, the following expression is then achieved:

$$\begin{aligned}
 \mu_m (A_{i+1} I_{m,i+1} - A_i I_{m,i}) + \eta_m (B_{j+1} I_{m,j+1} - B_j I_{m,j}) + \xi_m (C_{k+1} I_{m,k+1} - C_k I_{m,k}) \\
 + \frac{\alpha_{m+1/2} - \alpha_{m-1/2}}{w_m} = V_p [-(\kappa + \sigma_s) I_m + \kappa I_b + \sigma I_s]
 \end{aligned} \tag{5}$$

where the cell wall areas through which the radiation enters and leaves the cells are represented by  $A_i$ ,  $B_j$  and  $C_k$ , and the cell volume by  $V_p$ . The  $\alpha_{m\pm 1/2}$  terms are introduced to handle the discretization of the direction vector  $\eta$  and to correct for the curvature of the cylindrical furnace [22,38]. The six different cell surfaces for the two cell types are presented in Figure 3.

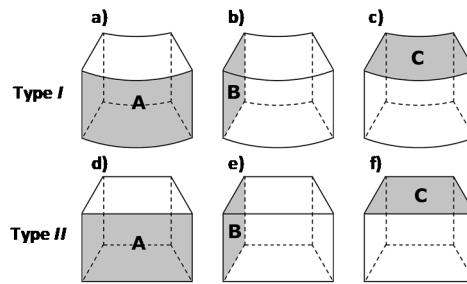


**Figure 3.** Surface areas present applying the discrete-ordinates method for a semi-cylindrical enclosure with a present bed material for cell types I (a–c) and II (d–f).

Defining the cells from a line between the center of the furnace and the middle of the bed surface, in the angular direction,  $r_{r,c}$  is the shortest distance from the central axis of the kiln to the bed surface. Each cell surface may then be expressed as:

$$\begin{aligned}
 A_{I,i} &= r_i \Delta \omega_j \Delta z_k & A_{II,i} &= r_{i,c} (\tan(\omega_{j+1}) - \tan(\omega_j)) \Delta z_k \\
 B_{I,j} &= \Delta r_i \Delta z_k & B_{II,j} &= \Delta r_i \Delta z_k \\
 C_{I,k} &= \pi (r_{i+1}^2 - r_i^2) \Delta \omega_j & C_{II,k} &= \frac{r_{i+1,c}^2 - r_{i,c}^2}{2} (\tan(\omega_{j+1}) - \tan(\omega_j))
 \end{aligned} \quad (6)$$

where  $i$ ,  $j$  and  $k$  represent the cell number in the radial, angular and axial direction, respectively, and  $\omega$  is the angle between two angular cells. The cell volume may be calculated as  $V_p = C_k \Delta z_k$  for both cell types. To find the  $\alpha_{m\pm 1/2}$  terms, a case in which divergenceless flow is assumed can be used according to Carlson and Lathrop [22], i.e., a case with neither intensity sources nor sinks, all intensities are alike and the right side of Equation (5) becomes zero. Considering the different cell surfaces, it may be observed that for cell type I,  $B_{j+1} = B_j$ , and for both cell types (I and II),  $C_{k+1} = C_k$ , while  $A_{i+1} \neq A_i$  for all cells.

$$\begin{aligned}
 \text{Type I} \quad & \alpha_{m+} I_{m+} - \alpha_{m-} I_{m-} = -w_m \mu_m (A_{i+1} I_{m,i+1} - A_i I_{m,i}) \\
 & \alpha_{m+} I_{m+} - \alpha_{m-} I_{m-} \\
 \text{Type II} \quad & = -w_m [\mu_m (A_{i+1} I_{m,i+1} - A_i I_{m,i}) \\
 & + \eta_m (B_{j+1} I_{m,j+1} - B_j I_{m,j})]
 \end{aligned} \quad (7)$$

To calculate the radiative intensities, an iterative solution process is required since the RTE is solved for each discrete angular direction, resulting in as many coupled partial differential equations. The iterative procedure starts at the wall at one end of the cylinder and, during the first iteration, values for the reflected and angular intensities are assumed, and thereafter updated in each iteration. The discretized rays are spread from the nodal points in the cells over spheres, and calculations are performed for one sphere octant at a time. With a beam directed from the wall towards the furnace center, the intensity to a node point  $P$  from one direction in an octant can be expressed as in Equation (8) [25].

$$I_{mP} = \frac{\mu_m A_i I_A + \eta_m B_j I_B + \xi_m C_k I_C + \frac{\alpha_m I_a}{w_m} + (\kappa I_b + \sigma_s I_{sca}) V_p}{\mu_m A_i + \eta_m B_j + \xi_m C_k + \frac{\alpha_m}{w_m} + (\kappa + \sigma_s) V_p} \quad (8)$$

The DOM may also suffer from false scattering, which may be reduced by using an appropriate spatial discretization scheme [23]. Here, a diamond differencing scheme is used to calculate the upstream intensities of  $I_A$ ,  $I_B$  and  $I_C$ . The diamond scheme is, however, known to have a shortcoming in eventually producing negative intensities. In the model, if any such negative value appears, it can be set to zero. It is also possible to ensure that these negative values never appear using a finite-difference weighting factor set to 1 as described by Fiveland [37].



In this work, using grey coefficients to represent the contributions from gases and particles, the RTE is solved for an overall (grey) intensity in order to reduce the required computational power. Considering the present gases, a weighted-sum-of-grey-gases (WSGG) model is used to estimate grey gas absorption coefficients for each cell in the model. Using a WSGG model (as first presented by Hottel and Sarofim [39]), the actual gases present in the furnace are represented by a mixture of a number of grey gases, where the contribution from each grey gas is connected to a weight depending on the real gas composition. Derived from the work of Johansson et al. [40], a modified WSGG model is used in this work, in which a set of four grey gases and one clear gas are applied, considering the gas concentrations of CO<sub>2</sub> and H<sub>2</sub>O. Spectral particle properties are calculated according to Mie theory for fuel and ash particles. Complex refractive indices from Foster and Howarth [41] are utilized for fuel particles, while a combination from the works of Lohi et al. [42], Gupta and Wall [43] and Goodwin and Mitchner [44] are utilized for ash particles. Present soot particles are considered to be small and Rayleigh theory is used to calculate the absorption coefficient with complex refractive indices from Chang and Charalampopoulos [45]. From particle size distributions, spectral absorption and scattering coefficients can be calculated for each particle type and size and summed to a single representative value of either coefficient. Using Planck averaging, the spectral particle properties can be turned into grey particle properties and used together with the WSGG model. A simplified scattering phase function is used in this work and cases assuming either pure isotropic or forward scattering (i.e., no scattering) are examined along with an additional case assuming 80% forward scattering, as suggested by Gronarz et al. [46]. A WSGG model was used previously for gases and coal particles together with the DOM by Yu et al. [47] for a cylindrical furnace of 3 m and 0.6 m inner diameter. They found that the DOM provides credible results of the calculated radiative heat transfer together with a WSGG model.

Once the RTE is solved for the furnace using the DOM, the incident radiative heat flux to the inner wall of the furnace can be calculated. This heat flux corresponds to the maximum radiative heat that can possibly be absorbed by a bed material in a rotary kiln. The incident radiative heat flux,  $q_r''$ , is calculated from the weighted sum of the incident radiation intensities from all directions, with  $\zeta_i$  representing any direction cosine, according to Equation (9) [48].

$$q_r'' = \sum_{i=1}^N I_i w_i \zeta_i \quad (9)$$

Depending on the absorptivity of the wall material surface, a portion of the incident radiative heat flux will be absorbed by the wall, heating the wall. If the conditions on the outside of the furnace, i.e., outer air and surrounding temperatures, are known, the inner wall temperature can be estimated from an energy balance of the heat transfer through the wall. At steady state conditions, the energy difference between the absorbed and emitted radiative heat must be transferred through the wall, neglecting convective heat transfer since radiation has been shown to dominate the total heat transfer on the inside of the furnace [32]. Further assuming grey and diffuse properties of the wall surface, i.e., absorptivity and emissivity are equal, the conductive heat transfer through the wall may be estimated according to Equation (10).

$$q_{con} = \frac{2\pi L k_w (T_w - T_{wo})}{n_z \ln\left(\frac{r_o}{r_i}\right)} = \varepsilon_w A_w (q_r'' - \sigma T_w^4) \quad (10)$$

where the outer wall temperature,  $T_{wo}$ , may be found from an energy balance over the furnace wall, since the heat transferred through the wall will at steady state be equal to the heat transfer, or rather heat loss, to the surroundings (at temperature  $T_\infty$ ) due to natural convection and radiation. Using



an overall heat transfer coefficient for the conductive heat transfer,  $k_w$ , based on the materials in the composite wall, the outer wall temperature may be estimated according to Equation (11) [32].

$$T_{ow} = T_w - \frac{(T_w - T_\infty) \frac{\ln\left(\frac{r_o}{r_i}\right)}{k_w}}{\frac{\ln\left(\frac{r_o}{r_i}\right)}{k_w} + \frac{1}{r_o} \left( \frac{1}{h_o} + \frac{1}{\varepsilon_o \sigma (T_o + T_\infty)(T_o^2 + T_\infty^2)} \right)} \quad (11)$$

Forced convection is neglected in the model since LKAB's kilns are shielded from wind by outer walls. The convective heat transfer coefficient for the natural convection on the outside of the pilot-scale furnace,  $h_o$ , can be expressed from the Nusselt number for a cylinder, as described by Churchill and Chu [49]:

$$Nu_D = \left( 0.60 + \frac{0.387 Ra_D^{1/6}}{\left[ 1 + \left( \frac{0.559}{Pr} \right)^{9/16} \right]^{8/27}} \right)^2 \quad (12)$$

The expression of Equation (12) is considered to be valid for  $Ra_D < 10^{12}$  [50]. By iterating the energy balance given in Equation (10), the inner and outer wall temperatures may be calculated from the incident heat flux and the outer wall heat loss, as well as an estimated temperature profile through the wall.

## 2.2. Data Gathering and Usage

The radiative heat transfer conditions in a rotary kiln have been experimentally examined by measuring the gas properties and particle concentration in a pilot-scale test furnace. The test furnace, as shown in Figure 4, is cylindrical and slightly tilting ( $3^\circ$  from the horizontal line), constructed as a down-scaled version of a full-scale rotary kiln used for iron ore pelletizing, applying constant velocity scaling [51], with a length of 4.8 m and an inner diameter of 650 mm. The inner wall was refractory lined, and an insulating material was used between the inner layer and the outer steel wall, with a total wall thickness of 285 mm. Probing and in-flame measurements were possible along the furnace axis due to 13 installed measurement ports, labeled MH 0–12, allowing for radially as well as axially distributed measurements within the furnace. The burner, positioned at the lower end of the furnace and in line with the furnace axis, had six registers for primary air and fuel and has been described more thoroughly by Edland et al. [52]. To mimic the full-scale process, where hot air from the product cooler section is used as secondary air to the kiln, large secondary air volumes of  $2300 \text{ Nm}^3/\text{h}$  at a temperature of approximately  $1050^\circ\text{C}$  were introduced through two large registers, one above and one below the burner, as described previously by Bäckström et al. [35]. The thermal input to the burner during the experimental campaign was  $580 \text{ kW}_{\text{th}}$  but no bed material was present, and the test furnace was stationary. The flue gases leave the furnace through an extended piping to a stack.

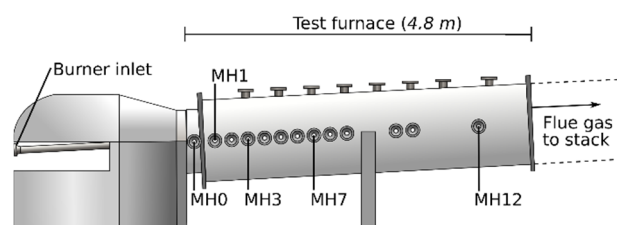


**Figure 4.** Schematic of the pilot-scale test furnace. Measurement ports (MH 0–12) are located along the axis of the furnace, allowing in-flame measurements, and the burner is located to the left.

Parameters measured during the experimental campaign included the radiative intensity using a narrow angle radiometer (NAR); radiative heat flux using an ellipsoidal radiometer; gas and wall

temperatures using a suction pyrometer with a type B thermocouple, an IR camera and stationary thermocouples; gas composition ( $\text{H}_2\text{O}$  and  $\text{CO}_2$ ) using a FTIR; and particle concentration and size distribution using a low-pressure impactor (size range 30 nm–10  $\mu\text{m}$ ). To achieve a good distribution of measurement positions along the furnace axis as well as the furnace diameter, measurements were focused on ports MH 0, 1, 3 and 7 for most parameters, while the IR camera was used for ports MH 0–10. Using water-cooled probes, measurements of temperature, gas composition and radiative intensity were gathered at several positions along the furnace diameter, while the incident radiative heat flux was measured at the position of the inner wall and the particle concentration at the centerline of the furnace. Performing radiative intensity measurements, quartz windows were placed in the opposite wall, acting as cold backgrounds to reduce background radiation along the furnace diameter and to better study the radiation from the flame. The temperature within the wall material was measured along the furnace axis, and thermocouples were positioned 70 mm within the wall from the inner surface. A more detailed description of the test furnace, the gathering of the data, the different measurement probes and techniques used can be found in [34].

Collected measurement data on temperature, gas composition, particle concentration and size distribution were used as input data for the model and prescribed at the cell nodes. Parameters were assumed to change linearly between two measurement positions, radially as well as axially, considering the linear temperature change in  $T^4$ . Values at the axial position of the burner were set from the measurements at port MH 0 and from the known secondary air inlet temperature and gas composition. Between the axial position of port MH 7 and the outlet of the furnace, the radial temperature was linearly changed to become isothermal at 1200 °C at the outlet and the gas composition was set to be the same as at the axial position of measurement port MH 7. Wall properties were set at the cell surface nodes but without available data concerning the solids radiative properties, the wall was assumed to be grey and diffuse. The lower end (burner position) and gas outlet/stack of the kiln were represented as two discs at the bottom and top ends of the cylinder, respectively, acting as boundaries in the DOM, with a set emissivity of 0.80. Several different fuels and fuel combinations of coal and biomass were tested in the furnace during the measurement campaign, though the modelling work in this paper is focused on a single case using a carbon-rich coal as fuel. The fuel particle concentration was known at the burner inlet and measured at the central position for ports MH 3 and 7. The collected and examined particle samples from the flame were found to contain small amount of ash in comparison to char and fuel particles. Ash particles were therefore neglected in the modelling work. Further, the ash contained a small amount of scattering components such as  $\text{Fe}_2\text{O}_3$  [53]—only approximately 5% of the ash was made up by  $\text{Fe}_2\text{O}_3$ . The char particle size distribution used in the modelling work was divided in 12 steps according to measurements. Further details on the measurement campaign, the different fuels examined and measurement data can be found in the work by Gunnarsson et al. [34].

### 3. Results and Discussion

To study the radiative heat transfer within the pilot-scale furnace, the described 3D model applying the DOM has been used as a tool in this work for a case using a carbon-rich coal at a thermal input of 580  $\text{kW}_{\text{th}}$ , and the results are compared to measurements. Using a grid resolution of  $30 \times 60 \times 100$ , the model was applied for the test furnace full length of 4.8 m, measured from the burner position. Extended temperature and gas concentration maps are shown in Figure 5, based on measurement data gathered at positions along the furnace diameter for several ports, where the measurement positions are indicated with asterisk (\*) symbols. Figure 5a–c shows cross-sectional temperature contour maps corresponding to the axial distances of ports MH 1, 3 and 7, as observed from the burner, and the estimated temperature in the whole furnace is shown in Figure 5d, as observed from above. Using an IR camera, the furnace inner wall temperature was estimated for ports MH 0–10 under the assumption of an isothermal wall for all angular positions for each axial position (Figure 5d). Downstream of port MH 10, the wall was assumed to be linearly decreasing to 1200 °C at the gas outlet. Figure 5e,f shows cross-sectional gas concentration maps of  $\text{CO}_2$  and  $\text{H}_2\text{O}$ , as observed from above the furnace.

During the experiments, radial symmetry of the flame within the furnace was aimed for but, as can be observed from the temperature maps, the flame became slightly tilted to the left from the burner. It should further be noted that since measurements were performed only along the horizontal line of the furnace, possible variations in the vertical direction could not be observed.

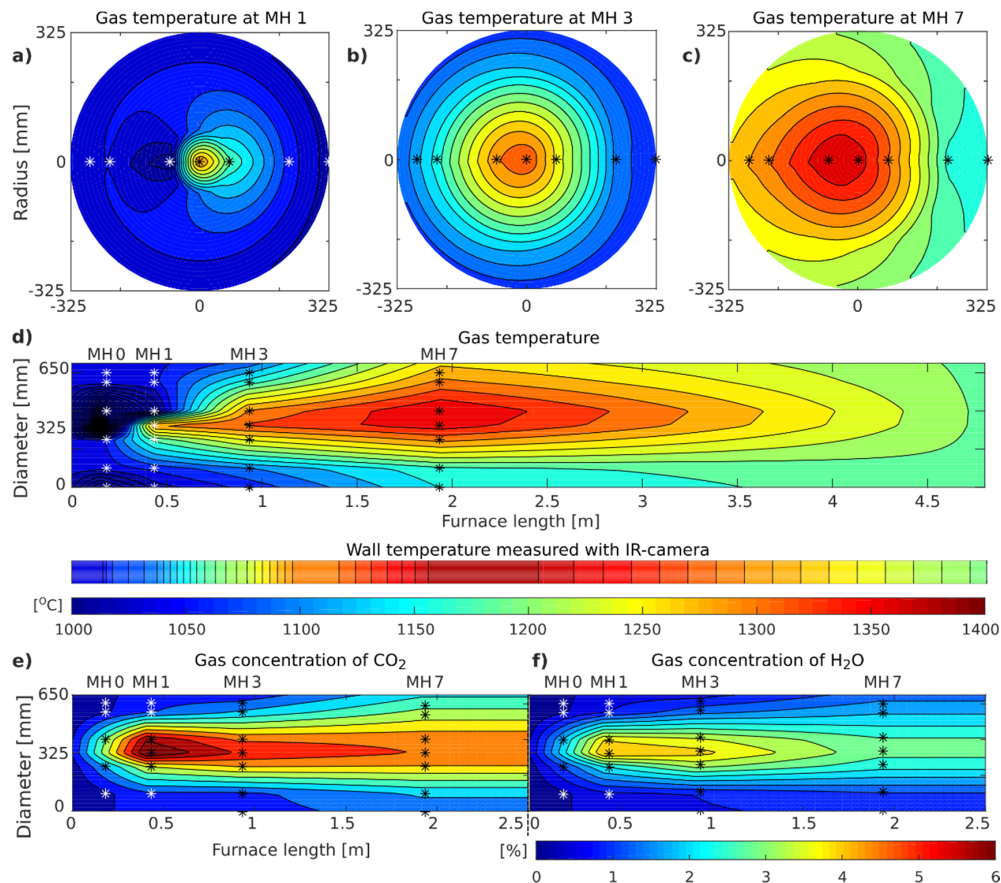


**Figure 5.** Cross-sectional maps of temperature and gas concentration based on measurements used as input data for the DOM. Temperatures, as seen from the burner position, for ports (a) MH 1, (b) MH 3, (c) MH 7 and (d) the whole furnace, as seen from above, including wall temperature measured with an infrared camera. Gas concentrations of (e) CO<sub>2</sub> and (f) H<sub>2</sub>O. Measurement positions are indicated with asterisk (\*) symbols.

The measured (triangles) as well as the modelled incident radiative heat fluxes along the furnace axis are shown in Figure 6a, with the burner located at the 0 m position, and the measurement data corresponding to ports MH 0, 1, 3 and 7. In the model, the scattering was set to be either isotropic (continuous line) or only forward (dashed line), but only marginal effects from the scattering assumption were observed; the isotropic and forward scattering predictions essentially lie on top of each other. This is probably mainly due to the relative size between the diameter and length of the furnace. It appears as if a large portion of the incident radiative heat flux to a position along the furnace axis originates from the flame and wall close to each axial position, minimizing particle scattering effects, and it is possible that the scattering would show a somewhat larger impact with an increased furnace diameter. At port MH 7, the model overestimates the radiative heat flux, which is most probably an effect of an overestimated wall temperature using the IR camera. Since radiation from the flame may be reflected in the wall and the wall emissivity is not fully known, estimations of the opposite furnace wall temperature using an IR camera is challenging. Further, at this axial position, the flame was slightly tilted towards the opposite wall of the furnace, causing an overestimation of the overall wall temperature assuming no angular variation of the wall temperature. Considering this, the model was

instead executed for a case where the wall temperature was assumed to adopt the temperature of the gas closest to the wall, according to Figure 5d—that is, for an overall colder wall with angular variations in temperature—and the modelled incident radiative heat flux is shown in Figure 6b. As can be observed, the difference between measured and modelled values is decreased for the downstream port MH 7 due to the cooler wall ( $\sim 110^\circ\text{C}$  at port MH 7). Figure 6c–e shows the measured radiative intensities for the respective ports MH 1, 3 and 7, indicated with triangles, and the modelled total radiative intensities, using the same assumptions as for Figure 6b. During the measurements, the NAR was traversed along the diameter of the furnace, entering through a measurement port. With the probe located at the inner wall, at the 0 mm position, high radiative intensities were measured due to the long path length of hot gases and particles in the probe's line of sight. Moving the probe through the flame and closer to the opposite wall, the measured radiative intensity decreases as the path length of hot gases and particles decreases. At the opposite wall (650 mm), the probe is directed towards a cold quartz glass in the furnace wall and the measured radiative intensity comes close to zero. In the model, this cold quartz glass is accounted for, allowing the wall to be cold at the specific and corresponding axial distance from the burner and for one angular position. Unlike the heat flux, large effects are apparent from the scattering assumption in the modelling of the radiative intensity. Assuming only forward scattering (continuous lines), i.e., no scattering, the radiative intensity is predicted satisfactorily for port MH 1 but underpredicted for ports MH 3 and 7. Instead assuming isotropic scattering (dashed lines), the model predicts the radiative intensity rather satisfactorily for all three ports. This increase in the modelled radiative intensity is due to the additional radiation scattered into the single direction studied with the NAR from the hot surrounding wall. That is, while assuming forward scattering, the only contribution to the total radiative intensity, in one narrow direction, originates from the emitting gases and particles present in the NAR's line of sight. An additional case, assuming the scattering phase function was 80% forward scattering (dotted line) and 20% isotropic scattering, was also studied and found to underestimate the radiative intensity at ports MH 3 and 7.

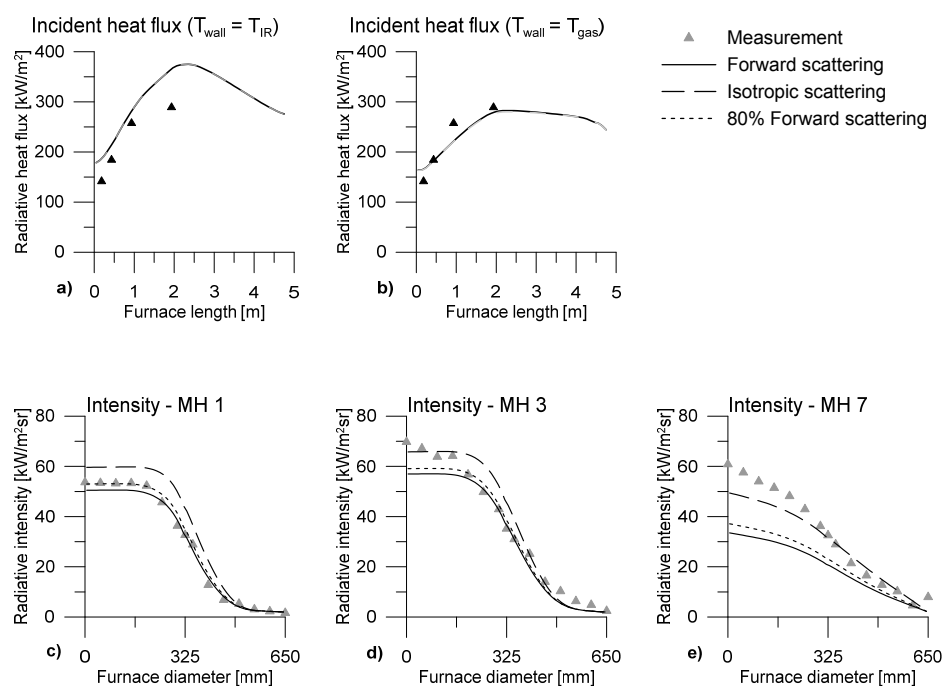


**Figure 6.** Measured (triangles) and modelled radiation assuming isotropic (dashed), forward (continuous) and 80% forward scattering (dotted). The incident radiative heat flux at the inner wall for measurement ports MH 0, 1, 3 and 7 along the furnace axis with the wall temperature set from (a) the IR camera and (b) the gas temperature closest to the wall. Measured and modelled radiative intensities along the furnace diameter at ports (c) MH 1, (d) MH 3 and (e) MH 7.

Solving the RTE and the energy balance expressed in Equation (10), in an iterative process, the inner and outer wall temperatures can be calculated from the set gas temperature, gas concentration and particle concentration within the test furnace. Figure 7a shows the calculated inner wall surface temperature along the furnace axis using the DOM as well as the estimated wall temperature using the infrared camera, the gas temperature close to the inner wall and the maximum flame temperatures based on measurements. Figure 7b shows the temperature of the inner and outer wall surfaces as well as the calculated and measured temperature at the intermediate position of 70 mm from the inside of the wall. The thermocouples were positioned along the axis of the furnace, beyond the insulation material, and as can be observed, the temperature drop appears within the insulation. The incident radiative heat flux for the calculated wall temperature profile is shown in Figure 7c, with good agreement to the measured values, and may be compared to Figure 6a,b. From the results shown in Figure 7, it appears that the estimated temperature using the infrared camera is in good agreement with the calculated wall temperature close to the burner, while it is closer to the maximum flame temperature farther downstream. It appears as reflected radiation was observed at the downstream measurement ports. At these downstream positions, the gas temperature closest to the wall is instead in good agreement with the calculated wall temperature. This could be considered to be in agreement with the observation of the flame being tilted towards the wall opposite of the measurement ports at these positions, as shown in Figure 5d.

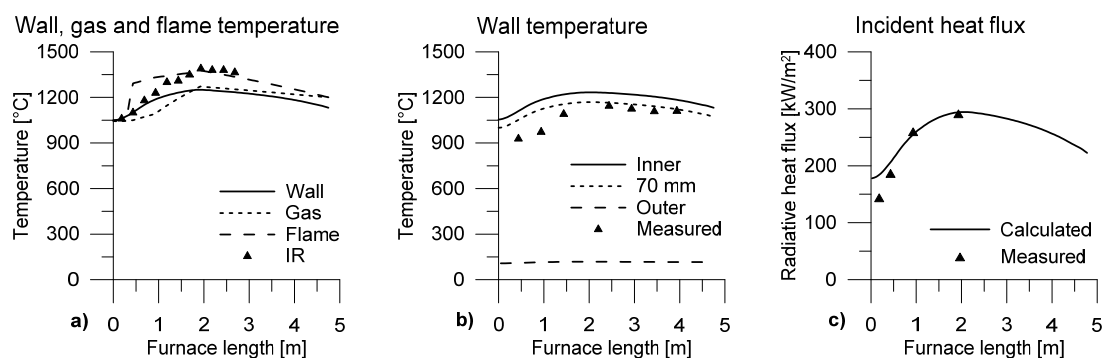


**Figure 7.** Measured (triangles) and modelled temperatures at the (a) inner wall, (b) inner, intermediate position at 70 mm from the inner surface of the wall and outer wall. (c) Measured (triangles) and modelled incident radiative heat flux at inner wall.

Regarding the modelled and underestimated radiative intensity at port MH 7, shown in Figure 6e, a better fit to the measurements could be achieved using the wall temperature as estimated with the infrared camera and assuming some particle scattering. However, considering the relatively large difference in the incident radiative heat flux at port MH 7, shown in Figure 6a, a more probable explanation is an underestimated number of particles at this axial position. Therefore, the impact on the radiative intensity and heat flux was studied, assuming the same case as in Figure 6b but changing the particle concentration at port MH 7. It was found that a 30% particle concentration increase at positions downstream of port MH 7 resulted in a rather good fit if isotropic scattering was assumed, while assuming forward scattering still underestimated the radiative intensity, as shown in Figure 8a. To illustrate the importance of considering the presence of particles, a case assuming no particles at all in the furnace was also examined and the radiative intensity is clearly reduced. Figure 8b shows the calculated incident radiative heat flux for those cases as well and the reduced heat flux due to the absence of particles is evident. Another explanation for the underestimated radiative intensity could be that the highest temperatures were observed at this axial position. Due to the difficulties of measuring accurate temperatures in coal flames, the measured flame temperature could actually be underestimated at this position.



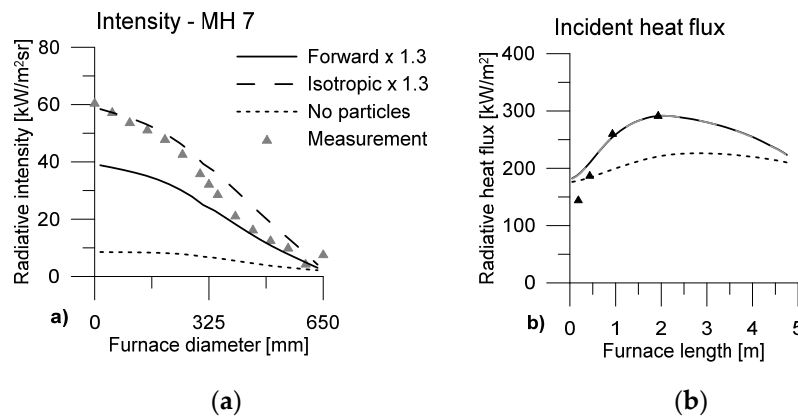


**Figure 8.** Measured and modelled (a) radiative intensity and (b) radiative heat flux showing the effects using an increased particle concentration with 30% as well as no particles.

While the wall temperature has been shown to have a relatively large effect on the incident heat flux, the wall emissivity could also be considered to have some effect. The wall emissivity was therefore varied from 0.80 to 0.60 and 1.00 for the inner wall surface. Figure 9 shows how the incident radiative heat flux varies with a varied wall emissivity and only marginal effects from the emissivity change can be observed, the predictions essentially lie on top of each other. The explanation for this is the small scale of the furnace, with a radius much smaller than the furnace length ( $0.325 \text{ m} \ll 4.8 \text{ m}$ ), the grey assumption of the wall material and the fact that it is a closed enclosure with a relatively small axial wall temperature gradient (see Figure 7a). Again, the largest portion of the incident radiative heat flux originates from the flame and wall close to each position (with a similar wall temperature) and after several surface reflections the radiosity (reflected and emitted radiation) from a surface comes close to black body radiation and becomes independent of the wall emissivity, if the radiative properties are assumed to be grey. That is, for a furnace with a larger radius, in comparison to the furnace length, the impact from the changed wall emissivity may become more evident, and more affected from the set end boundaries.

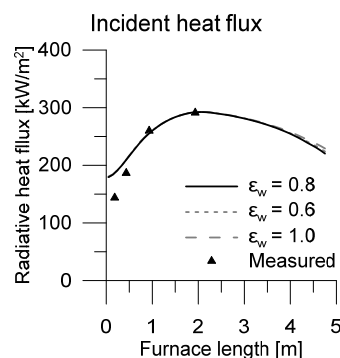


**Figure 9.** Measured and modelled incident radiative heat flux varying the inner wall emissivity from 0.8 to 0.6 and 1.0.

The model also has the ability to include a bed material, introducing cells of Type II; see Figure 1. Figure 10a,b shows the incident radiative heat flux to the furnace wall for a case with an additional bed material, in which the bed material accounts for approximately 10% of the furnace volume, as the full-scale furnace used by LKAB. The cylindrical furnace wall has been flattened out in the figures and the presence of the bed material is indicated, close to the top of each figure. In Figure 10a the wall and bed temperatures are assumed to be equal to the closest gas temperatures, while in Figure 10b a made-up case is considered in which a bed is introduced at  $100^\circ\text{C}$  at the axial position of 4.8 m and leaves with a temperature of  $1050^\circ\text{C}$  at the burner (0 m), i.e., equal to the secondary air inlet

temperature, in an attempt to imitate, e.g., a bed of pellets being heated as it is moving through the kiln, though with a much larger temperature gradient. The bed and wall emissivities were both set to 0.80 in this example. To more easily compare the two cases, the gas composition and temperature profiles were simplified to be radially symmetric—that is, profiles from Figure 5d–f (0–325 mm along the diameter) were used for all angular positions at each axial position, and forward scattering was used. As expected, when adding a cold bed material to the kiln, the maximum incident radiative heat flux is clearly visibly lowered in Figure 10b: the overall incident radiative heat flux at all surfaces is reduced. It may also be observed that the radiative heat flux is higher to the cold bed material than to the surrounding wall at the same axial position. This example illustrates the possibility to use the model to study the effect of different parameter changes.

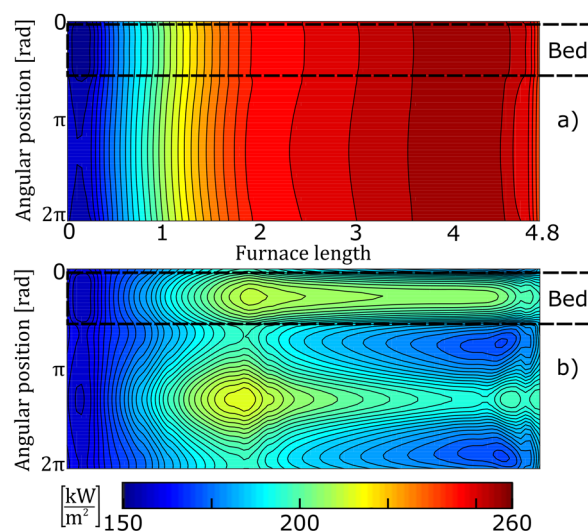


**Figure 10.** Modelled incident radiative heat flux to the furnace wall and the introduced bed material. The bed temperature is set to (a) the closest gas temperature; (b) a linear increase from 100 °C at the furnace outlet (right end) to 1050 °C at the burner (left end).

#### 4. Conclusions

A discrete-ordinates method has been applied to develop a 3D model of the radiative heat transfer in cylindrical and semi-cylindrical enclosures in order to resemble rotary kilns with a present bed material. Experimentally gathered data from a pilot-scale test furnace, comprising temperature, gas composition and particle concentration, were used as input data for the model and the modeled radiative heat fluxes were compared to measurements with satisfactory agreement.

The wall temperature was found to have a significant impact on the radiative heat flux, whereas the inner wall emissivity only showed a marginal impact due to the relation between the furnace radius and axial length as well as the assumption of grey radiative properties. The inner wall temperature and the incident radiative heat flux were calculated in an iterative process from the prescribed properties in the freeboard using Equation (10), including conduction through the furnace wall as well as heat losses from the cylindrical outside of the test furnace, and provided good results when compared to measurements. The intermediate wall temperature was also estimated in a satisfactory way when compared to the measurements from the thermocouples positioned within the wall, 70 mm from the inner surface of the wall. The radiative intensity was found to be underestimated in the model when scattering was neglected. Instead assuming isotropic scattering, the model predicted the measured radiative intensity quite well, since radiation was then scattered into the measured direction (with the NAR) from the hot surrounding wall. The impact on the radiative heat flux from the presence of particles in the freeboard was also examined by varying the particle load.



Though no experiments including a bed material in the furnace were performed in this work, the possibility of introducing a bed material to the model was demonstrated, and the effect on the overall radiative heat flux of a cold bed material was examined. As could be expected, the overall radiative heat flux to the bed and wall was reduced when a cold bed material was introduced to the furnace, but the radiative heat flux was found to be higher to the bed material than to the surrounding wall at the same axial position.

The model demonstrated the possibility to study radiative heat transfer in full-scale rotary kilns in future work, using different fuels such as oil or coal, and performing desirable operational sensitivity analyses.

**Author Contributions:** Conceptualization, A.G. and K.A.; funding acquisition, K.A. and C.F.; investigation, A.G.; methodology, A.G.; project administration, K.A.; software, A.G.; supervision, K.A. and B.R.A.; visualization, A.G.; writing—original draft, A.G.; writing—review and editing, K.A., B.R.A. and C.F. All authors have read and agreed to the published version of the manuscript.

**Funding:** LKAB and the Swedish Energy Agency are acknowledged for the financial support of this work (project number 47223327).

**Acknowledgments:** LKAB is acknowledged for providing the experimental setup and for the inspiring collaboration.

**Conflicts of Interest:** The authors declare no conflict of interest.

## Nomenclature

$A$	cell area in radial direction	$\theta$	polar angle
$B$	cell area in angular direction	$\Delta\omega$	cell angle
$C$	cell area in axial direction	$\kappa$	absorption coefficient
$\hat{i}, \hat{j}, \hat{k}$	unit vectors in Cartesian coordinates	$\nu$	wave number
$I$	radiative intensity	$\sigma$	Stefan-Boltzmann constant
$I$	cell type	$\sigma_s$	scattering coefficient
$II$	cell type	$\phi$	scattering phase function
$k_w$	conductive heat transfer coefficient	$\Phi$	azimuthal angle
$L$	furnace length	$\psi$	space variable
$n$	number of cells	$\Omega$	solid angle
$N$	total number of directions used		
$Nu$	Nusselt number		
$r$	radius		
$Pr$	Prandtl number		
$q$	heat transfer		
$q''$	radiative heat flux		
$Ra$	Rayleigh number		
$\hat{s}$	unit vector in a given direction		
$T$	temperature		
$V$	cell volume		
$w$	angular quadrature weight		

## Greek Symbols

$\alpha$	angular derivative coefficient
$\Delta\omega$	cell angle
$\varepsilon$	emissivity
$\zeta, \eta, \mu, \xi$	direction cosine

## Subscripts

$b$	black body
$con$	conductive heat transfer
$D$	furnace diameter
$i$	radial position
$j$	angular position
$k$	axial position
$m$	discrete direction
$o$	outer
$P$	node point
$r$	radial cell
$w$	wall
$z$	axial cell
$\infty$	ambient

## References

1. Boateng, A.A. *Rotary Kilns Transport. Phenomena and Transport. Processes*; Butterworth-Heinmann: Oxford, UK, 2008.
2. Cross, M.; Young, R.W. Mathematical model of rotary kilns used in the production of iron ore pellets. *Ironmak. Steelmak.* **1976**, *3*, 129–137.
3. Gorog, J.P.; Brimacombe, J.K.; Adams, T.N. Radiative heat transfer in rotary kilns. *Met. Trans. B* **1981**, *12*, 55–70. [[CrossRef](#)]
4. Gorog, J.P.; Adams, T.N.; Brimacombe, J.K. Regenerative Heat Transfer in Rotary Kilns. *Met. Trans. B* **1982**, *13*, 153–163. [[CrossRef](#)]
5. Gorog, J.P.; Adams, T.N.; Brimacombe, J.K. Heat Transfer from Flames in a Rotary Kiln. *Met. Trans. B* **1983**, *14*, 411–424. [[CrossRef](#)]
6. Thornton, G.J.; Batterham, R.J. The Transfer of Heat in Kilns. In Proceedings of the Tenth Australian Chemical Engineering Conference, Sydney, Australia, 24–26 August 1982; pp. 260–266.
7. Barr, P.V.; Brimacombe, J.K.; Watkinson, A.P. A Heat-Transfer Model for the Rotary Kiln: Part I. Pilot Kiln Trials. *Met. Mater. Trans. B* **1989**, *20*, 391–402. [[CrossRef](#)]
8. Barr, P.V.; Brimacombe, J.K.; Watkinson, A.P. A heat transfer model for the rotary kiln: Part II. Development of the cross section model. *Met. Mater. Trans. B* **1989**, *20*, 403–419. [[CrossRef](#)]
9. Boateng, A.A.; Barr, P.V. A thermal model for the rotary kiln including heat transfer within the bed. *Int. J. Heat Mass Transf.* **1996**, *39*, 2131–2147. [[CrossRef](#)]
10. Herz, F.; Mitov, I.; Specht, E.; Stanev, R. Influence of the Motion Behavior on the Contact Heat Transfer Between the Covered Wall and Solid Bed in Rotary Kilns. *Exp. Heat Transf.* **2015**, *28*, 174–188. [[CrossRef](#)]
11. Wes, G.W.J.; Drinkenburg, A.A.H.; Stermerding, S. Heat Transfer in a Horizontal Rotary Drum Reactor. *Powder Technol.* **1976**, *13*, 185–192. [[CrossRef](#)]
12. Li, S.Q.; Ma, L.B.; Wan, W.; Yao, Q. A mathematical model of heat transfer in a rotary kiln thermo-reactor. *Chem. Eng. Technol.* **2005**, *28*, 1480–1489. [[CrossRef](#)]
13. Njeng, S.A.B.; Vitu, S.; Clausse, M.; Dirion, J.; Debacq, M. Wall-to-solid heat transfer coefficient in flighted rotary kilns: Experimental determination and modeling. *Exp. Ther. Fluid Sci.* **2018**, *91*, 197–213. [[CrossRef](#)]
14. Tscheng, S.H.; Watkinson, A.P. Convective Heat Transfer in a Rotary Kiln. *Can. J. Chem. Eng.* **1979**, *57*, 433–443. [[CrossRef](#)]
15. Specht, E. *Heat and Mass Transfer in Thermoprocessing*; Vulkan Verlag GmbH: Essen, Germany, 2017.
16. Georgallis, M.; Nowak, P.; Salcudean, M.; Gartshore, I.S. Modelling the Rotary Lime Kiln. *Can. J. Chem. Eng.* **2008**, *83*, 212–223. [[CrossRef](#)]
17. Mujumdar, K.S.; Ranade, V.V. CFD modeling of rotary cement kilns. *Asia-Pac. J. Chem. Eng.* **2008**, *3*, 106–118.
18. Mouangue, R.; Ngako, S.; Tégawendé Zaida, J.; Kuitche, A. Heavy Fuel Oil Combustion in a Cement Rotary Kiln: Measurement and Modelling. *Ind. Combust. J. Int. Flame Res. Found.* **2020**, 1–29.
19. Witt, P.J.; Sinnott, M.D.; Cleary, P.W.; Schwarz, M.P. A hierarchical simulation methodology for rotary kilns including granular flow and heat transfer. *Min. Eng.* **2018**, *119*, 244–262. [[CrossRef](#)]
20. Forsmo, S.P.E.; Forsmo, S.-E.; Samskog, P.-O.; Björkman, B.M.T. Mechanisms in oxidation and sintering of magnetite iron ore green pellets. *Powder Technol.* **2008**, *183*, 247–259. [[CrossRef](#)]
21. Jonsson, C.Y.C.; Stjernberg, J.; Wiinikka, H.; Lindblom, B.; Boström, D.; Öhman, M. Deposit formation in a grate-kiln plant for iron-ore pellet production. Part 1: Characterization process gas particles. *Energy Fuels* **2013**, *27*, 6159–6170. [[CrossRef](#)]
22. Carlson, B.G.; Lathrop, K.D. Transport Theory The Method of Discrete Ordinates. In *Computing Methods in Reactor Physics*; Greenspan, H., Kelber, C.N., Okrent, D., Eds.; Gordon and Breach Science Publishers: New York, NY, USA, 1968; pp. 171–265.
23. Coelho, P.J. Advances in the discrete ordinates and finite volume methods for the solution of radiative heat transfer problems in participating media. *J. Quant. Spectrosc. Radiat. Transf.* **2014**, *145*, 121–146. [[CrossRef](#)]
24. Jamaluddin, A.S.; Smith, P.J. Predicting Radiative Transfer in Axisymmetric Cylindrical Enclosures Using the Discrete Ordinates Method. *Combust. Sci. Technol.* **1988**, *62*, 173–186. [[CrossRef](#)]
25. Jamaluddin, A.S.; Smith, P.J. Discrete-Ordinates Solution of Radiative Transfer Equation in Nonaxisymmetric Cylindrical Enclosures. *J. Ther. Heat Transf.* **1992**, *6*, 242–245. [[CrossRef](#)]

26. Kim, M.Y.; Baek, S.W. Modeling of radiative heat transfer in an axisymmetric cylindrical enclosure with participating medium. *J. Quant. Spectrosc. Radiat. Transf.* **2005**, *90*, 377–388. [\[CrossRef\]](#)
27. Adams, B.R.; Smith, P.J. Three dimensional discrete ordinates modelling of Radiative transfer in a geometrically complex furnace. *Combust. Sci. Technol.* **1993**, *88*, 293–308. [\[CrossRef\]](#)
28. Byun, D.Y.; Baek, S.W.; Kim, M.Y. Investigation of Radiative Heat Transfer in Complex Geometries Using Blocked-Off, Multiblock, and Embedded Boundary Treatments. *Numer. Heat Transf.* **2003**, *43*, 807–825. [\[CrossRef\]](#)
29. Seo, S.-H.; Kim, T.-K. Study on Interpolation Schemes of the Discrete Ordinates Interpolation Method for Three-Dimensional Radiative Heat Transfer with Nonorthogonal Grids. *J. Heat Transf.* **1998**, *120*, 1091–1094. [\[CrossRef\]](#)
30. Howell, L.H.; Beckner, V.E. A Discrete Ordinates Algorithm for Domains with Embedded Boundaries. *J. Ther. Heat Transf.* **1997**, *11*, 549–555. [\[CrossRef\]](#)
31. Liu, J.; Shang, H.M.; Chen, Y.S.; Wang, T.S. Prediction of Radiative Transfer in General Body-Fitted Coordinates. *Numer. Heat Transf.* **1997**, *31*, 423–439. [\[CrossRef\]](#)
32. Gunnarsson, A.; Andersson, K.; Adams, B.R.; Fredriksson, C. Full-scale 3D-modelling of the radiative heat transfer in rotary kilns with a present bed material. *Int. J. Heat Mass Transf.* **2019**, *147*. [\[CrossRef\]](#)
33. Gunnarsson, A.; Andersson, K.; Bradley, A. 3D-Modelling of the Radiative Heat Transfer in Rotary Kilns with a Present Bed Material. In Proceedings of the 6th International Conference on Computational Thermal Radiation in Participating Media, Cascais, Portugal, 11–13 April 2018.
34. Gunnarsson, A.; Bäckström, D.; Johansson, R.; Fredriksson, C.; Andersson, K. Radiative Heat Transfer Conditions in a Rotary Kiln Test Furnace Using Coal, Biomass, and Cofiring Burners. *Energy Fuels* **2017**, *31*, 7482–7492. [\[CrossRef\]](#)
35. Bäckström, D.; Johansson, R.; Andersson, K.; Wiinikka, H.; Fredriksson, C. On the use of alternative fuels in rotary kiln burners—An experimental and modelling study of the effect on the radiative heat transfer conditions. *Fuel Process. Technol.* **2015**, *138*, 210–220. [\[CrossRef\]](#)
36. Modest, M.F. *Radiative Heat Transfer*, 3rd ed.; Elsevier: Amsterdam, The Netherlands, 2013.
37. Fiveland, W.A. Three-Dimensional Radiative Heat-Transfer Solutions by the Discrete-Ordinates Method. *J. Ther. Heat Transf.* **1988**, *2*, 309–316. [\[CrossRef\]](#)
38. Liu, J.; Shang, H.M.; Chen, Y.S. Development of an unstructured radiation model applicable for two-dimensional planar, axisymmetric, and three-dimensional geometries. *J. Quant. Spectrosc. Radiat. Transf.* **2000**, *66*, 17–33. [\[CrossRef\]](#)
39. Hottel, H.C.; Sarofim, A.F. *Radiative Transfer*, 1st ed.; McGraw-Hill, Inc.: New York, NY, USA, 1967.
40. Johansson, R.; Leckner, B.; Andersson, K.; Johnsson, F. Account for variations in the H<sub>2</sub>O to CO<sub>2</sub> molar ratio when modelling gaseous radiative heat transfer with the weighted-sum-of-grey-gases model. *Combust. Flame* **2011**, *158*, 893–901. [\[CrossRef\]](#)
41. Foster, P.J.; Howarth, C.R. Optical Constants of Carbons and Coals in the Infrared. *Carbon* **1968**, *6*, 719–729. [\[CrossRef\]](#)
42. Lohi, A.; Wynnkyj, J.R.; Rhodes, E. Spectral measurement of the complex refractive index of fly ashes of canadian lignite and sub-bituminous coals. *Can. J. Chem. Eng.* **1992**, *70*, 751–758. [\[CrossRef\]](#)
43. Gupta, R.P.; Wall, T.F. The optical properties of fly ash in coal fired furnaces. *Combust. Flame* **1985**, *61*, 145–151. [\[CrossRef\]](#)
44. Goodwin, D.G.; Mitchner, M. Flyash Radiative Properties and Effects on Radiative Heat-Transfer in Coal-fired Systems. *Int. J. Heat Mass Transf.* **1989**, *32*, 627–638. [\[CrossRef\]](#)
45. Chang, H.; Charalampopoulos, T.T. Determination of the Wavelength Dependence of Refractive Indices of Flame Soot. *Proc. R. Soc. A Math. Phys. Eng. Sci.* **1990**, *430*, 577–591. [\[CrossRef\]](#)
46. Gronarz, T.; Schulze, J.; Laemmerhold, M.; Graeser, P.; Gorewoda, J.; Kez, V.; Habermehl, M.; Schiemann, M.; Ströhle, J.; Epple, B.; et al. Quantification of the influence of parameters determining radiative heat transfer in an oxy-fuel operated boiler. *Fuel Process. Technol.* **2017**, *157*, 76–89. [\[CrossRef\]](#)
47. Yu, M.J.; Baek, S.W.; Kang, S.J.A.E. Modeling of Pulverized Coal Combustion with Non- Gray Gas Radiation Effects. *Combust. Sci. Technol.* **2001**, *166*, 151–174. [\[CrossRef\]](#)
48. Modest, M.F. The Method of Discrete Ordinates (SN-Approximation). In *Radiative Heat Transfer*, 3rd ed.; Elsevier: Amsterdam, The Netherlands, 2013; pp. 541–584.

49. Churchill, S.W.; Chu, H.H.S. Correlating Equations for Laminar and Turbulent Free Convection from a Horizontal Cylinder. *Int. J. Heat Mass Transf.* **1975**, *18*, 1049–1053. [[CrossRef](#)]
50. Incropera, F.P.; Dewitt, D.P.; Bergman, T.L.; Lavine, A.S. Free Convection. In *Principles of Heat and Mass Transfer*; John Wiley & Sons, Inc.: Hoboken, NJ, USA, 2013; pp. 594–652.
51. Weber, R. Scaling characteristics of aerodynamics, heat transfer, and pollutant emissions in industrial flames. *Symp. Combust.* **1996**, *26*, 3343–3354. [[CrossRef](#)]
52. Edland, R.; Normann, F.; Fredriksson, C.; Andersson, K. Implications of Fuel Choice and Burner Settings for Combustion Efficiency and NO<sub>x</sub> Formation in PF-Fired Iron Ore Rotary Kilns. *Energy Fuels* **2017**, *31*, 3253–3261. [[CrossRef](#)]
53. Im, K.H.; Ahluwalia, R.K. Radiation properties of coal combustion products. *Int. J. Heat Mass Transf.* **1993**, *36*, 293–302. [[CrossRef](#)]



© 2020 by the authors. Licensee MDPI, Basel, Switzerland. This article is an open access article distributed under the terms and conditions of the Creative Commons Attribution (CC BY) license (<http://creativecommons.org/licenses/by/4.0/>).